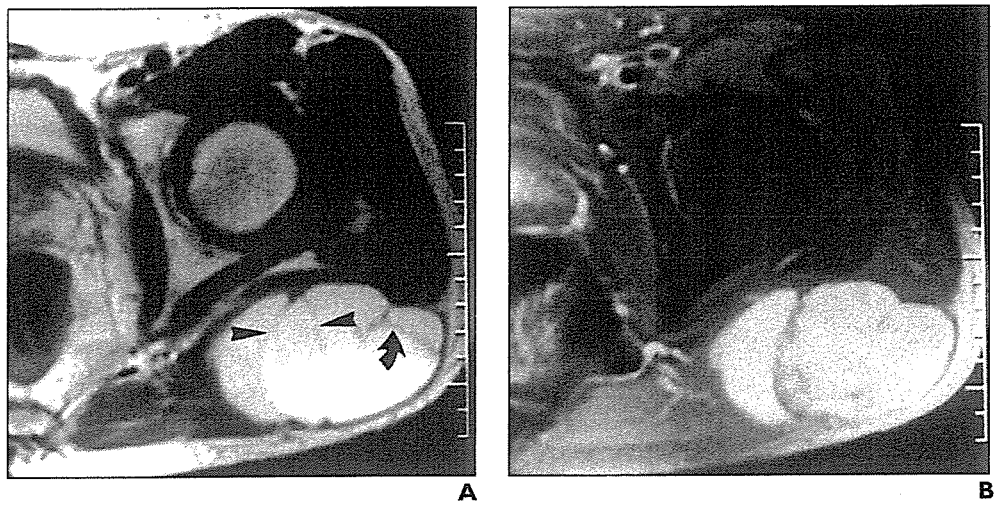

A B

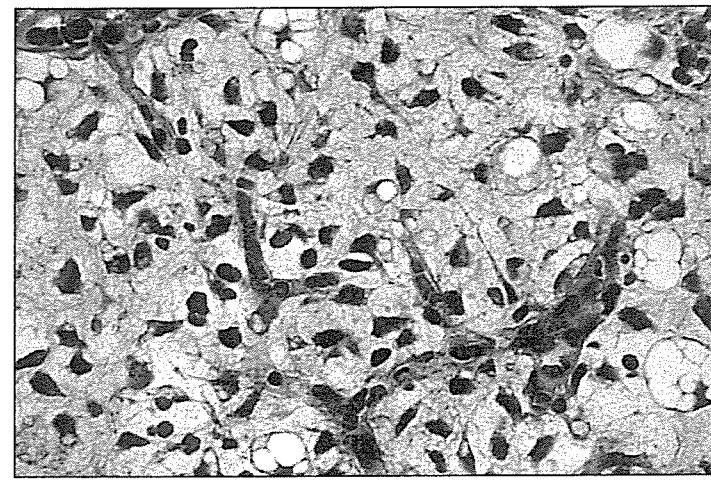

C

Fig. 2.—62-year-old man with low-grade myxoid–round cell liposarcoma in left buttock.
A, Axial T2-weighted fast spin-echo MR image (TR/TE, 3,500/100) shows septate appearance of lesion. Linear structures of low intensity contained thick septa (*arrow*) and thin septa (*arrowheads*).
B, Axial fat-saturated contrast-enhanced T1-weighted spin-echo MR image (720/20) shows tumor of high intensity with slight enhancement of septa.
C, Photomicrograph of specimen shows paucicellular myxoid liposarcoma with less than 25% round cell components has dispersed small round or short spindled cells and multivacuolated lipoblasts within abundant myxoid matrix and plexiform vascular network. (H and E, ×200)

ulated morphology. On MR images, thin and thick septa (Fig. 2) were identified in 31 (86.1%) and 10 (27.8%) tumors, respectively. On T1-weighted MR images the signals of the tumors relative to those of muscle were hyperintense ($n = 15$), isointense ($n = 12$), or hypointense ($n = 9$). Tumors showed predominantly increased signal intensity compared with that of the skeletal muscle on T2-weighted MR images. The images showed the tumor as having a heterogeneous appearance with thin or thick septa of low intensity. High-intensity signals similar to subcutaneous fatty tissue (high-intensity signal pattern) were found in 15 tumors (41.7%) on both T1- and T2-weighted MR images (Figs. 1 and 4).

On contrast-enhanced MR images, pronounced enhancement (Fig. 4) located mostly at the peripheries of the lesions was present in 22 tumors (61.1%). Globular and nodular enhancement (Figs. 3 and 4) was found mostly in the centers of the lesions of 16 patients (44.4%), whereas diffuse enhancement (Fig. 1) was seen in six lesions (16.7%). Contrast-enhanced MR images also revealed that 23 tumors (63.9%) had homogeneously enhanced tumor capsules (Fig. 3).

All tumors were characterized microscopically by a prominent plexiform vascular pattern admixed with an abundant myxoid matrix. The extent of cellularity ranged from slight to moderate, and the lesions were composed of small uniform, round, or spindle-shaped hyperchromatic cells. Tumor necrosis was found on microscopic observation in 12 cases (33.3%). The necrotic areas varied in degree, but most tumors contained only a small amount of necrotic areas that were difficult to identify on MR images.

Statistically significant MRI findings that favored a diagnosis of intermediate- or high-grade tumor were large tumor size (> 10 cm) ($p < 0.01$), deeply situated tumor ($p < 0.05$), tumor possessing irregular contours ($p < 0.001$), absence of lobulation ($p < 0.001$), absence of thin septa ($p < 0.05$), presence of thick septa ($p < 0.01$), absence of tumor capsule ($p < 0.001$), high-intensity signal pattern ($p < 0.01$), pronounced enhancement ($p < 0.001$), and globular and nodular enhancement ($p < 0.001$). The presence of thin septa or a tumor capsule indicates low-grade tumor. Irregular contours were found in only 10 high-grade tumors (58.8%). All the low-grade tumors had a capsule, thin septa, and a high-intensity signal pattern. The odds ratios for a specific finding favoring a diagnosis of intermediate- or high-grade tumor are shown in Table 1. The multiple logistic regression model showed that irregular contour and thick septa were the most significant predictors of intermediate- or high-grade tumors, with an odds ratio of 13.8 for both (95% confidence interval [CI], 1.5–128.8; $p < 0.05$).

At the last follow-up, 10 (27.8%) of the 36 patients had died of their disease and four (11.1%) were alive with metastatic disease. The 5- and 10-year survival rates were 80.5%

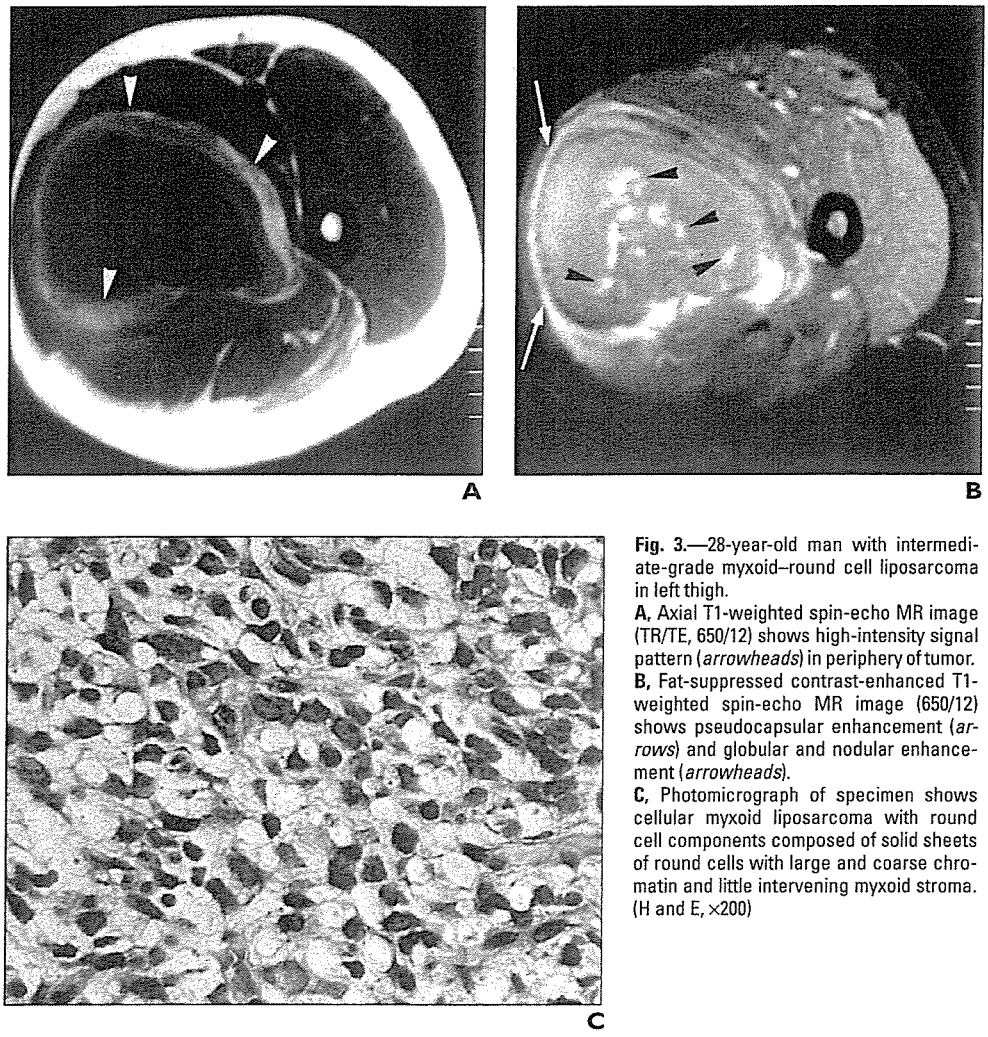

Fig. 3.—28-year-old man with intermediate-grade myxoid–round cell liposarcoma in left thigh.
A, Axial T1-weighted spin-echo MR image (TR/TE, 650/12) shows high-intensity signal pattern (*arrowheads*) in periphery of tumor.
B, Fat-suppressed contrast-enhanced T1-weighted spin-echo MR image (650/12) shows pseudocapsular enhancement (*arrows*) and globular and nodular enhancement (*arrowheads*).
C, Photomicrograph of specimen shows cellular myxoid liposarcoma with round cell components composed of solid sheets of round cells with large and coarse chromatin and little intervening myxoid stroma. (H and E, ×200)

and 72.4%, respectively. The univariate analysis showed that thin septa ($p < 0.05$), tumor capsule ($p < 0.01$), and pronounced enhancement ($p < 0.01$) were significantly associated with overall survival (Table 2). The multivariate analysis revealed that pronounced enhancement was the most significant adverse prognostic factor (Fig. 5) with a relative risk of 7.3 (95% CI, 1.5–35.1; $p < 0.05$).

TABLE 1 Odds Ratio for Features Favoring Diagnosis of Intermediate- or High-Grade Myxoid–Round Cell Liposarcoma

Feature	Odds Ratio	95% CI
Size > 10 cm	9.0	2.6–30.9
Lobulation absent	21.0	8.3–126.5
Thick septa present	20.3	2.1–188.7
Pronounced enhancement present	34.7	3.72–324.1
Globular and nodular enhancement present	9.0	2.0–41.3

Note.—CI = confidence interval.

Discussion

In this study, we documented the prognostic significance of MRI features in patients with myxoid–round cell liposarcomas. Univariate analysis revealed that the presence of thin septa, a tumor capsule, and pronounced enhancement had a significant correlation with overall survival. Multivariate analysis showed that, of these variables, pronounced enhancement on contrast-enhanced MR images was the most influential adverse prognostic factor. This MRI finding of enhancement correlated with the round cell–component content on pathologic specimens. The prognostic importance of the round cell component has been acknowledged in previous studies [18–20]. From a practical viewpoint, detection of this enhancement pattern on contrast-enhanced MR images in myxoid–round cell liposarcomas is useful for predicting their behavior.

The amount of necrosis has been reported to be correlated with clinical outcome [21–25]. Spontaneous tumor necrosis identified in four (4%) of 95 patients with myxoid–round cell liposarcomas was correlated with increased risks of metastasis and death [18]. In our study, we did not evaluate the relationship between the presence of tumor necrosis and patient prognosis, because most tumors accompanied by necrosis in our study contained only a small amount of necrotic areas that were difficult to identify on MR images.

On contrast-enhanced MR images, pronounced enhancement was located mainly at the periphery of the lesion in 61.1% of the pa-

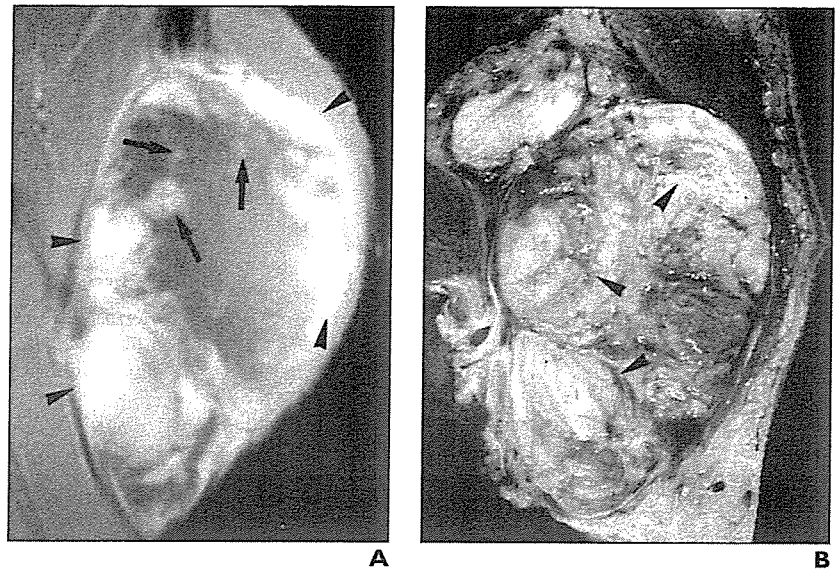

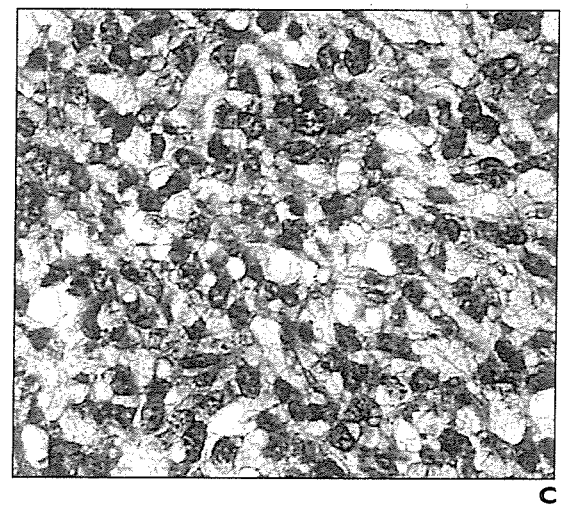

Fig. 4.—69-year-old man with high-grade myxoid–round cell liposarcoma in left thigh.
A, Sagittal contrast-enhanced T1-weighted spin-echo MR image (TR/TE, 600/15) shows globular and nodular enhancement (*arrows*) and pronounced enhancement (*arrowheads*) predominantly at tumor periphery.
B, Photograph of macroscopic specimen of same tumor as in **A** shows heterogeneous tumor components (*arrowheads*).
C, Photomicrograph shows that specimen is composed of solid sheets of uniform round cells with large and coarse chromatin. (H and E, ×200)

tients, and globular and nodular enhancement occurred at the lesion center in 44.4%. These two patterns of enhancement were characteristic of intermediate- or high-grade tumors. Round cell components were reported to be located at the peripheries of lobules; adjacent to fibrous septa extending through the tumor; and surrounding large vessels, particularly in tumors with only a small amount of round cell components [7, 8]. Thus, these two enhancement patterns may be reliable imaging findings for detecting round cell components within tumors. In one study, despite a small sample size, researchers showed that patients (n = 5) who initially had a tumor with 5% or greater round cell components had a significantly higher incidence of metastasis or death from disease than those (n = 7) who initially had a tumor with less than 5% round cell components [18]. In a study of 24 patients with round cell components composing 25% or more of the tumor, round cell components were associated significantly with a lower survival rate [19]. However, the correlation between the quantity of round cell components and the clinical outcome may depend on the difficulty in quantifying the round cell components at transitional areas at microscopic observation.

There was no significant difference between the risks of an adverse outcome in patients with myxoid and transitional areas without round cell components and those with myxoid areas alone [19]. The pathologic variables responsible for differences among observers in identifying round cell components are considered to be numerous and include inaccurate criteria for tissue processing and selection of the assessment area within the spectrum of myxoid–round cell liposarcomas [20]. Our results suggest that contrast-enhanced MR images can assist in detecting round cell component content within the entire tumor and assist in the distinction of low-grade and of intermediate- or high-grade myxoid–round cell liposarcomas.

In previous reports [26–29], the descriptions of the enhancement patterns identified on MR images included little enhancement or a few patterns (i.e., heterogeneous, homogeneous, no enhancement). However, the end points selected in these prior studies depended simply on the pathologic diagnosis of "myxoid liposarcoma," and the investigators were unaware of the lineage of "myxoid–round cell liposarcoma" as a disease entity. The results of our study are based on a definite diagnosis of myxoid–round cell liposarcoma, and we stress that

TABLE 2 MRI Findings and Univariate Analyses of Survival in 36 Cases of Myxoid–Round Cell Liposarcoma

MRI Findings	No. (%) of Cases	5-Year Survival Rate (%)	p^a
Size (cm)			0.10
≤ 10	20 (55.6)	84.2	
> 10	16 (44.4)	56.8	
Depth			0.26
Superficial	5 (13.9)	100	
Deep	31 (86.1)	66.7	
Contour			0.27
Regular	26 (72.2)	71.2	
Irregular	10 (27.8)	62.5	
Lobulation			0.19
Absent	20 (55.6)	59.8	
Present	16 (44.4)	85.2	
Thin septa			0.02
Absent	5 (13.9)	26.7	
Present	31 (86.1)	77.1	
Thick septa			0.47
Absent	26 (72.2)	66.7	
Present	10 (27.8)	72.3	
Tumor capsule			< 0.01
Absent	13 (36.1)	16.6	
Present	23 (63.9)	83.1	
Pronounced enhancement			< 0.01
Absent	14 (38.9)	100	
Present	22 (61.1)	54.9	
Globular and nodular enhancement			0.91
Absent	20 (55.6)	78.4	
Present	16 (44.4)	66.8	
High-intensity signal pattern			0.71
Absent	21 (58.3)	72.4	
Present	15 (41.7)	69.1	

[a]Log-rank test.

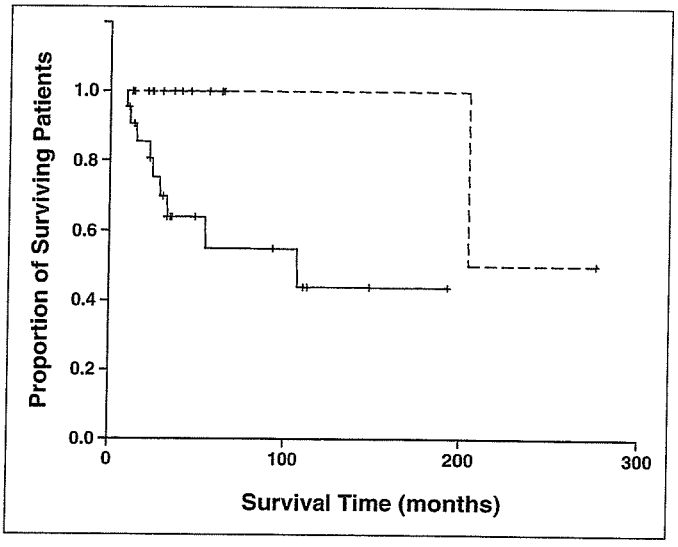

Fig. 5.—Graph shows Kaplan-Meier survival curve according to presence (*solid line*) or absence (*dashed line*) of pronounced enhancement on contrast-enhanced MR images for 36 patients with myxoid–round cell liposarcomas.

the presence of globular and nodular or pronounced enhancement identified on MRI is a finding suggestive of intermediate- or high-grade tumor and reflects the amount of round cell components in the tumor, which strongly affects patient outcome.

The presence of linear or amorphous hyperintense foci behaving like fatty tissue on T1-weighted MR images has been reported to be a pattern suggestive of myxoid liposarcoma [27]. Myxoid–round cell liposarcoma often consists of multiple histologic subtypes in the same lesion. We observed a high-intensity signal pattern in 15 low-grade tumors, and this finding was consistent with immature fatty tissue or the fat components of the tumors. Immature spindle cells lacking obvious fat genesis may be seen next to multivacuolated lipoblasts. Although MRI is sensitive enough to detect minute fat deposits or immature fatty components, our univariate analysis showed no significant association between high-intensity signal pattern on MR images and survival [28, 29].

In summary, the spectrum of MRI findings in myxoid–round cell liposarcomas is continuous. MRI findings can assist in the distinction between low-grade and intermediate- or high-grade myxoid–round cell liposarcomas. MRI findings that favored a diagnosis of intermediate- or high-grade tumor included large (> 10 cm) size of tumor, deeply situated tumor, tumor possessing irregular contours, absence of lobulation, absence of a tumor capsule, absence of thin septa, presence of thick septa, high-intensity signal pattern, pronounced enhancement, and globular and nodular enhancement. The presence of thin septa or a tumor capsule indicates low-grade tumor. Imaging features associated with overall survival were thin septa, a tumor capsule, and pronounced enhancement. Multivariate analysis showed that pronounced enhancement on MRI is the most significant factor in predicting an adverse prognosis for patients with myxoid–round cell liposarcoma.

References

1. Enzinger FM, Weiss SW. *Soft tissue tumors*, 4th ed. St. Louis, MO: Mosby–Year Book, 2001: 670–687
2. Enzinger FM, Winslow DJ. Liposarcoma: a study of 103 cases [in German]. *Virchows Arch Path Anat Physiol Klin Med* 1962;335:367–388
3. Evans HL. Liposarcoma: a study of 55 cases with a reassessment of its classification. *Am J Surg Pathol* 1979;3:507–523
4. Evans HL. Liposarcomas and atypical lipomatous tumors: a study of 66 cases followed for a minimum of 10 years. *Surg Pathol* 1988;1:41–54

5. Hashimoto H, Enjoji M. Liposarcoma: a clinicopathologic subtyping of 52 cases. *Acta Pathol Jpn* 1982;32:933–948
6. Knight JC, Renwick PJ, Cin PD, Van den Berghe H, Fletcher CD. Translocation t(12;16)(q13;p11) in myxoid and round cell liposarcoma: molecular and cytogenetic analysis. *Cancer Res* 1995;55:24–27
7. Panagopoulos I, Mandahl N, Ron D, et al. Characterization of the *CHOP* breakpoints and fusion transcripts in myxoid liposarcomas with the 12;16 translocation. *Cancer Res* 1994;54:6500–6503
8. Kuroda M, Ishida T, Horiuchi H, et al. Chimeric *TLS/FUS-CHOP* gene expression and the heterogeneity of its junction in human myxoid and round cell liposarcoma. *Am J Pathol* 1995;147: 1221–1227
9. Hisaoka M, Tsuji S, Morimitsu Y, et al. Detection of *TLS/FUS-CHOP* fusion transcripts in myxoid and round cell liposarcomas by nested reverse transcription-polymerase chain reaction using archival paraffin-embedded tissues. *Diagn Mol Pathol* 1998;7:96–101
10. Jelinek JS, Kransdorf MJ, Shmookler BM, Aboulafia AJ, Malawer MM. Liposarcoma of the extremities: MR and CT findings in the histologic subtypes. *Radiology* 1993;186:455–459
11. London J, Kim EE, Wallace S, Shirkhoda A, Coan J, Evans H. MR imaging of liposarcomas: correlation of MR features and histology. *J Comput Assist Tomogr* 1989;15:832–835
12. Sundaram M, Baran G, Merenda G, McDonald DJ. Myxoid liposarcoma: MR imaging appearances with clinical and histological correlation. *Skeletal Radiol* 1990;19:359–362
13. Ramsdell MG, Chew FS, Keel SB. Myxoid liposarcoma of the thigh. *AJR* 1998;170:1242
14. Sung MS, Kang HS, Suh JS, et al. Myxoid liposarcoma: appearance at MR imaging with histologic correlation. *RadioGraphics* 2000;20:1007–1019
15. Hasegawa T, Yokoyama R, Lee YH, et al. Prognostic relevance of a histological grading system using MIB-1 for adult soft-tissue sarcoma. *Oncology* 2000;58:66–74
16. Hasegawa T, Yamamoto S, Yokoyama R, et al. Prognostic significance of grading and staging systems using MIB-1 score in adult patients with soft tissue sarcoma of the extremities and trunk. *Cancer* 2002;95:843–851
17. Hasegawa T, Yamamoto S, Nojima T, et al. Validity and reproducibility of histologic diagnosis and grading for adult soft-tissue sarcomas. *Hum Pathol* 2002;33:111–115
18. Kilpatrick SE, Doyon J, Choong PFM, et al. The clinicopathologic spectrum of myxoid and round cell liposarcoma: a study of 95 cases. *Cancer* 1996;77:1450–1458
19. Smith TA, Easley KA, Goldblum JR. Myxoid/round cell liposarcoma of the extremities: a clinicopathologic study of 29 cases with particular attention to extent of round cell liposarcoma. *Am J Surg Pathol* 1996;20:171–180
20. Antonescu CR, Tschernyavsky SJ, Decuseara R, et al. Prognostic impact of p53 status, *TLS-CHOP* fusion transcript structure, and histological grade in myxoid liposarcoma: molecular and clinicopathologic study of 82 cases. *Clin Cancer Res* 2001;7:3977–3987
21. Lack EE, Steinberg SM, White DM, et al. Extremity soft tissue sarcomas: analysis of prognostic variables in 300 cases and evaluation of tumor necrosis as a factor in stratifying high-grade sarcomas. *J Surg Oncol* 1989;41:263–273
22. Mandard AM, Petiot JF, Marnay J, et al. Prognostic factors in soft tissue sarcomas: a multivariate analysis of 109 cases. *Cancer* 1989;63:1437–1451
23. Choong PFM, Gustafson P, Willen H, et al. Prognosis following locally recurrent soft tissue sarcoma: a staging system based on primary and recurrent tumor characteristics. *Int J Cancer* 1995;60:33–37
24. Orson GG, Sim FH, Reiman HM, et al. Liposarcoma of the musculoskeletal system. *Cancer* 1987;60:362–370
25. Reitan JB, Kaazhus O, Brenhoud IO, et al. Prognostic factors in liposarcoma. *Cancer* 1985;55: 2482–2490
26. Arkun R, Memis A, Akalin T, Ustun EE, Sabah D, Kandiloglu G. Liposarcoma of soft tissue: MRI findings with pathologic correlation. *Skeletal Radiol* 1997;26:167–172
27. Munk PL, Lee MJ, Janzen DL, et al. Lipoma and liposarcoma: evaluation using CT and MR imaging. *AJR* 1997;169:589–594
28. Kransdorf MJ. Malignant soft tissue tumors in a large referral population: distribution of diagnoses by age, sex, and location. *AJR* 1995;164: 129–134
29. Kransdorf MJ, Murphey MD. Radiologic evaluation of soft-tissue masses: a current perspective. *AJR* 2000;175:575–587

ORIGINAL ARTICLE

ACTA RADIOLOGICA

Percutaneous Transhepatic Portal Vein Embolization: Effectiveness of Absolute Ethanol Infusion with Balloon Catheter in a Pig Model

M. SATAKE, U. TATEISHI, T. KOBAYASHI, S. MURATA & T. KUMAZAKI

Division of Diagnostic Radiology, National Cancer Center Hospital and Department of Radiology, Nippon Medical School, Tokyo, Japan

Satake M, Tateishi U, Kobayashi T, Murata S, Kumazaki T. Percutaneous transhepatic portal vein embolization: effectiveness of absolute ethanol infusion with balloon catheter in a pig model. Acta Radiol 2005;46:000–000.

Purpose: To evaluate the effectiveness of portal vein embolization (PVE) with absolute ethanol using multidetector-row computed tomography (CT) angiography in a pig model.

Material and Methods: Percutaneous transhepatic PVE with 10 ml absolute ethanol was performed in liver segments ($n=5$) or subsegments ($n=5$) in 10 pigs. CT images and volumetric data were qualitatively and quantitatively assessed to determine future liver remnant (FLR) hypertrophy and to correlate with histopathologic changes 2–6 weeks after PVE. Effectiveness evaluation was based on changes in absolute FLR size and ratio of FLR to total estimated liver volume (TELV).

Results: Occlusion of the embolized vessel was achieved immediately after injecting absolute ethanol within a range of 0.25–0.33 ml/kg. The TELV prior to PVE was 660.49 ± 103.66 cm^3 (range 527.22 to 833.70 cm^3) and after PVE 769.51 ± 29.36 cm^3 (range 685.95 to 887.34 cm^3). The mean FLR/TELV ratio increase after PVE was 14.2%. No statistically significant difference was found in the increase of TELV between segmental or subsegmental PVE. On microscopic observation, atrophy of the embolized liver was noted in all animals and was seen distinctly at 3 weeks after PVE in 2 animals.

Conclusion: Both regenerative response and histopathologic changes of the liver were seen after PVE with absolute ethanol with a mean FLR/TELV ratio of 14.2%.

Key words: Absolute ethanol; balloon catheter; embolization; portal vein

Ukihide Tateishi, M.D., Ph.D., Division of Diagnostic Radiology, National Cancer Center Hospital, Tsukiji, Chuo-Ku, 104-0045, Tokyo, Japan (fax. +81 3 3542 3815, e-mail. utateish@ncc.go.jp)

Accepted for publication February 2005

Percutaneous transhepatic portal vein embolization (PVE) of the liver leads to atrophy of the embolized lobe and compensatory hypertrophy of the remnant liver, which may prevent liver failure after hepatic resection (17). The PVE procedure minimizes the risk of portal vein thrombosis and contralateral vascular injury to the future liver remnant (FLR). PVE is performed mainly in the preoperative treatment of selected patients who are potential candidates for major hepatic resections (2, 5, 11, 12, 14, 18). By inducing selective lobar hypertrophy of the normal liver, PVE may reduce complications after major resections (2, 5, 11, 12, 14, 18).

The substances used for embolization include coils (5), microspheres (5), cyanoacrylate and ethiodized oil (6), gelatin (6, 19), polyvinyl alcohol (PVA) particles (7, 16), and absolute ethanol (4, 10, 15, 20–22). Absolute ethanol is one of the most reliable agents for achieving atrophy of the embolized lobes and induces histopathologic changes in the embolized liver that lead to periportal necrosis and fibrosis (4, 10, 15, 20–22). The hypertrophy of the remnant liver segments observed in previous studies almost certainly represents hepatic regeneration, but we know of no experimental studies in which hepatic regeneration after PVE with absolute ethanol has been evaluated by CT angiography (1, 5). The purpose of this study was to evaluate the effectiveness of PVE with absolute ethanol in pigs by correlating the CT angiographic findings with the histopathologic observations.

Taylor & Francis
Taylor & Francis Group

DOI 10.1080/02841850510021328

Material and Methods

Procedure

Ten female domestic pigs (Saitama Experimental Animal Supply, Saitama, Japan) weighing 30.0 to 35.0 kg were used in this study. The study protocol was approved by our institutional animal study committee. Animals were sedated and anesthetized by premedication with an intramuscular injection of 15 mg/kg ketamine-HCl (Sankyo, Tokyo, Japan), 2 mg/kg atropine sulfate (Yamanouchi, Tokyo, Japan), and 4 mg/kg 4′-fluoro-4-butyrophenone (Sankyo, Tokyo, Japan), and ventilated with administration of 50–100 mg thiamylal sodium (Yoshitomi, Tokyo, Japan). The anesthesia was maintained mainly by inhalation of sevoflurane (Maruishi, Tokyo, Japan). Intravenous ketamine-HCl and pancronium bromide (Sankyo, Tokyo, Japan) were also administered to maintain anesthesia when necessary. 0.5 g Cefazolin sodium (Fujisawa, Tokyo, Japan) was administered intravenously to prevent infection. A catheter was inserted into a femoral artery with a 5 Fr. super-sheath introducer set (Medikit, Tokyo, Japan). Under fluoroscopic guidance, a 6 Fr. super-sheath introducer (Medikit, Tokyo, Japan) was transhepatically introduced into a branch of the right portal venous system. A 0.035-inch guide-wire (Radifocus Guide Wire, Terumo, Tokyo, Japan) and a 0.035-inch Amplatz guide-wire (Cook Medical, Bloomington, Ill., USA) were used to secure access, and the 6 Fr. vascular sheath was placed with a 5 Fr. dilator.

Digital subtraction portography was performed with a 5 Fr. angiographic balloon catheter (Clinical Supply, Gifu, Japan) inserted into the main portal vein, which was identified by injecting 5–10 ml of contrast material (Iopamiron 370 mgI/ml; Nihon Schering, Osaka, Japan) during suspended respiration. Portal vein branches were embolized by injection with from 5 to 10 ml of absolute ethanol into a 5 Fr. balloon catheter within the portal vein branches supplying the segments targeted. The balloon catheter was used to block the embolized branches and prevent reflux. After embolization of the targeted segments, the catheter was positioned in the main portal vein, and a portogram was obtained. The portal vein catheter was thereafter left in place as an indwelling.

Selective embolization of segment IV was performed in three pigs, segment VI in two pigs, the anterior segment in two pigs, the posterior segment in two pigs, and the lateral segment in one pig. Blood samples were collected and serum creatinine, total serum bilirubin, serum alkaline phosphatase, serum lactate dehydrogenase, serum aspartate aminotransferase, and serum alanine aminotransferase levels were measured before and after embolization. The blood ethanol concentration was also determined before and 3, 5, 10, 15, 20, 30, and 60 min after embolization.

CT examinations

The animals were sedated with sevoflurane, ketamine-HCl, and pancronium bromide before receiving a propofol infusion. The animals were placed in the CT scanner in the supine position. All CT images were obtained with a multidetector-row CT system (Aquilion V-detector CT; Toshiba, Tokyo, Japan), and the following scan parameters were used: axial 4 slice mode, 2.0 mm collimation, 0.5 s/rotation, 120 kVp, 150 mA/rotation, 30–40 cm of field of view, and 512×512 matrix. Images were reconstructed using standard algorithms with 5 mm section thickness on a display window width of 300–350 Hounsfield Units (HU) and a window center of 120–180 HU. A 5 Fr. cobra-type femoral artery catheter (Clinical Supply, Gifu, Japan) was first placed in the superior mesenteric artery for CT arterial portography (CTAP) and then repositioned in the common hepatic artery for CT hepatic arteriography (CTHA). CTAP was performed with scan delays of 10 s (early-phase) and 35 s (delayed-phase) after injection of the 1:2 diluted contrast material (Iopamiron 370 mgI/ml; Nihon Schering, Osaka, Japan). CTHA was also performed with scan delays of 10 s (early-phase) and 35 s (delayed-phase). The contrast material was injected with a dedicated CT injector (Autoenhance A250; Nemoto Kyorindo, Tokyo, Japan) at a flow rate of 2.0 ml/s, and a total volume of 60 ml for each scan. Both CTAP and CTHA were performed before and 60 min after the embolization procedure in all animals. Follow-up CT (CTAP and CTHA) was performed after 2 ($n=5$) and 3 ($n=5$) weeks. The interval between PVE and scarification ranged from 2 to 6 weeks: 2 weeks ($n=5$), 3 weeks ($n=2$), 4 weeks ($n=1$), and 6 weeks ($n=2$).

Image analysis

Two radiologists interpreted all of the CT images by consensus. All CTAP images were evaluated for the morphology of portal trunk and branches, the presence of portal occlusion and recanalization, perfusion defects, and periportal hyperattenuation. All CTHA images were also evaluated for the presence of normal or abnormal hepatic arterial perfusion. The extent of perfusion defects or periportal hyperattenuation on CTAP images and

hepatic arterial perfusion on CTHA patterns was recorded based on the following grading system: grade 0, normal; grade 1, no more than 25% of the embolized segment involved; grade 2, 26–50% of the embolized segment involved; grade 3, 51–75% of the embolized segment involved; grade 4, 76–100% of the embolized segment involved.

CTAP images were used to calculate liver volume before and after PVE. The 3-dimensional models of the whole liver were reconstructed on a workstation (Ziosoft M900, Quadra, v. 3.10f; Ziosoft Inc., Tokyo, Japan). Threshold limits were applied to exclude soft tissue surrounding the liver by using a standard algorithm mode that manipulates a voxel matrix of 512×512 pixels. The portal vein, biliary tract, and gastrointestinal structures were selectively removed from the model. The embolized fraction of the liver was calculated by measuring the enhanced and non-enhanced areas and dividing the sum of volumes that were not enhanced by the volume of the entire liver. The percentage of voxels with attenuation values below a specified level was defined as the lower attenuation volume. The initial evaluation of the FLR was performed by consensus between two radiologists and was based on calculation of the total estimated liver volume (TELV) on cross-sectional images. TELV was estimated before PVE and follow-up. In addition, a second evaluation of the FLR and TELV was performed by another radiologist to assess reproducibility.

Histopathologic examinations

On the day of sacrifice, the animals were given an intravenous dose of ketamine-HCl, and portography was performed via the indwelling portal vein catheter. Tissue specimens were immediately collected from each lobe of the liver. Tissue wedges from each lobe of the liver were fixed in 10% neutral buffered formalin and were prepared for paraffin embedding and sectioning. A series of 4-μm-thick sections was prepared, mounted on slides, and stained with either hematoxylin-eosin or Masson trichrome. All pathologic specimens were evaluated by one pathologist.

Statistical analysis

Paired t tests were used to determine whether any of the changes in TELV, FLR/TELV ratio, or serum concentrations were statistically significant. Correlation between the serum concentrations of the substances analyzed and the areas of PVE or the duration after PVE and the correlation between the weight of the liver and TELV were assessed by Pearson's correlation coefficients. The agreement between the CT findings was assessed by using weighted kappa statistics. The kappa statistics and 95% confidence intervals (CIs) were calculated as a measure of agreement. The kappa statistic was interpreted thus: 0.00 to 0.20, slight agreement; 0.21 to 0.40, fair agreement; 0.41 to 0.60, moderate agreement; 0.61 to 0.80, substantial agreement; and 0.80 to 1.00, almost perfect agreement. The significance criterion for all tests was set at the $P < 0.05$ level.

Results

Imaging findings

PVE was technically successful in all pigs. Occlusion of the embolized vessel was achieved immediately after the injection of absolute ethanol, and the doses ranged from 0.25 to 0.33 ml/kg. No inflow of portal blood into the embolized portal branches was detected by portography after PVE (Fig. 1). No constriction or obstruction of unembolized vessels was observed.

Early-phase CTAP revealed that the embolized portal branches were dilated by wedge infusion during balloon occlusion (Fig. 2). Late-phase CTAP showed slight obliteration of the embolized branches in all animals (Fig. 2). There was no CT evidence of portal vein recanalization in any of the animals. Perfusion defects in the embolized liver (mean grade 3.0) were identified on CTAP in all animals (Fig. 3). Late-phase CTAP showed periportal hyperattenuation of the embolized portal branches (mean grade 0.7) in 70.0% of the animals (Fig. 4). Both early- and late-phase CTHA were performed after PVE, and parenchymal enhancement in the embolized liver was observed in all animals (Fig. 3).

Findings at follow-up CTAP and CTHA after 2 or 3 weeks demonstrated severe atrophy of the embolized parts of the liver (Fig. 5). Complete occlusion of portal branches without recanalization was found in all animals. The areas of the embolized liver with periportal hyperattenuation on CTAP became completely atrophic, which showed almost perfect agreement (weighted Kappa 0.87; 95% CI: 0.73–1.00). Perfusion defects in the embolized liver were identified on CTAP, and the mean grade was 3.4. CTHA also showed parenchymal enhancement of the embolized liver in all animals. The agreement between the perfusion defects on CTAP and the hepatic arterial hyperperfusion on CTHA was almost perfect (weighted kappa 0.84; 95% CI: 0.67–0.94).

Blood samples and CT volumetry

Complications were not recorded in any animal, and the course after PVE was uneventful. All laboratory

Acta Radiologica rad60237.3d 6/4/05 17:08:04

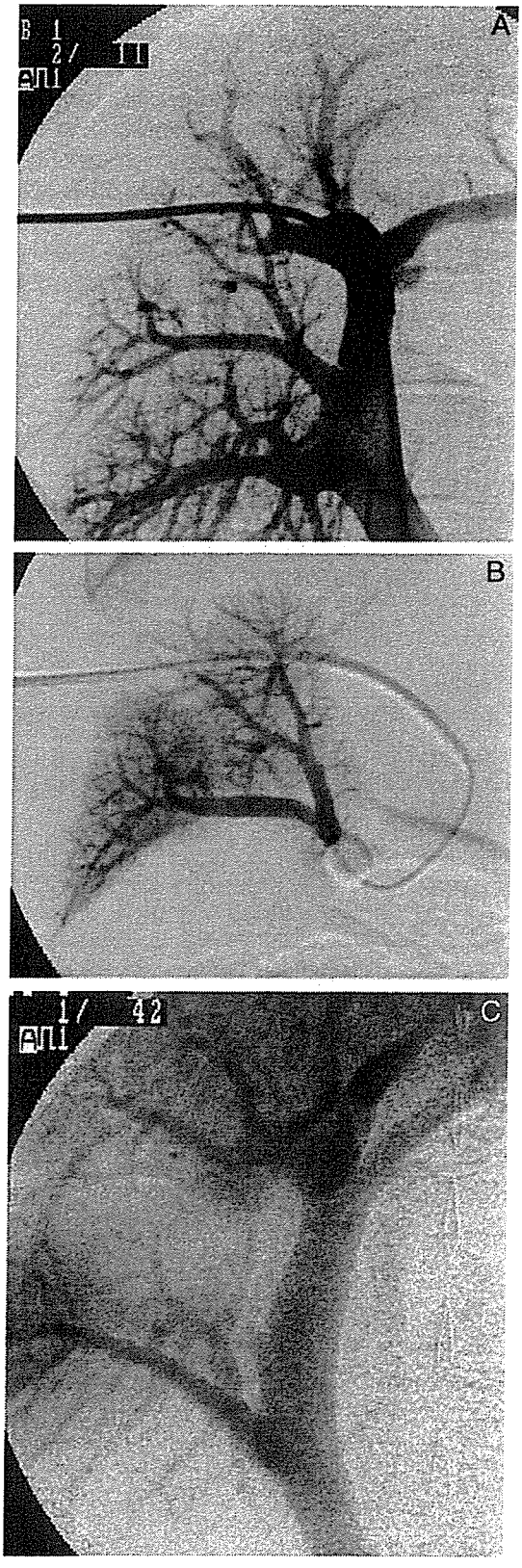

Fig. 1. Percutaneous transhepatic portal vein embolization (PVE) of the posterior portal branches of the right lobe. A. Digital subtraction portography before PVE. B. Digital subtraction portography of the posterior portal branches during balloon occlusion. C. Portography after PVE shows total occlusion of the posterior branches of the right lobe.

values determined to detect hepatic or renal damage were in the normal range before PVE. Statistically significant increases were observed in the serum concentrations of the liver transaminases, alanine aminotransferase, and lactic acid dehydrogenase (Table 1). The serum concentration of alanine aminotransferase depended not only on the interval after PVE ($P<0.0001$), but also on the size of the PVE areas ($P<0.05$). The serum lactic acid dehydrogenase concentration was also dependent on the interval after PVE ($P<0.05$), but not on the size of the PVE areas. No statistically significant correlation were found between PVE areas and serum concentrations of the substances measured including aspartate aminotransferase, the bile canalicule marker alkaline phosphatase, total bilirubin, or creatinine. The average serum ethanol concentration decreased after PVE (range 0.51 mg/dl [3 min] – 0.25 mg/dl [60 min]).

The TELV prior to PVE was 660.49 ± 103.66 cm^3 (range 527.22 to 833.70 cm^3) and the TELV after PVE was 769.51 ± 29.36 cm^3 (range 685.95 to 887.34 cm^3). The increase in TELV after PVE was 109.01 ± 44.94 cm^3. The mean increase in FLR/TELV ratio after PVE was 14.2%. There was a statistically significant correlation between liver weight and TELV after PVE ($r=0.964$, $P<0.0001$). No statistically significant difference was found between the results of initial and second calculation of TELV.

Histopathologic findings

Grossly, the embolized liver appeared yellowish, and contained mass-like (Fig. 6) or amorphous (Fig. 7) areas, predominantly in the parenchyma surrounding Glisson's capsule. Atrophy of the embolized liver was noted in all animals and was seen distinctly at 3 weeks after PVE in 2 animals. Hypertrophy of the unembolized liver was evident at least 2 weeks after PVE. Microscopic examination revealed degenerated hepatocytes with intact lobular architecture in the mass-like areas of the embolized liver (Fig. 8). No hepatic blood perfusion was observed in the sinusoids in tissue fixed with absolute ethanol. Inflammatory infiltration accompanied by giant cells and parenchymal necrosis was seen mainly in the sinusoids at 3–6 weeks after PVE. The portal veins were dilated and occluded with fresh emboli in the amorphous areas in the embolized lobes. Mononuclear cell infiltration was observed in Glisson's capsule without destruction of the hepatic lobule at least 2 weeks after PVE. Degenerated hepatocytes in the embolized lobes were much more likely to be eosinophilic and to

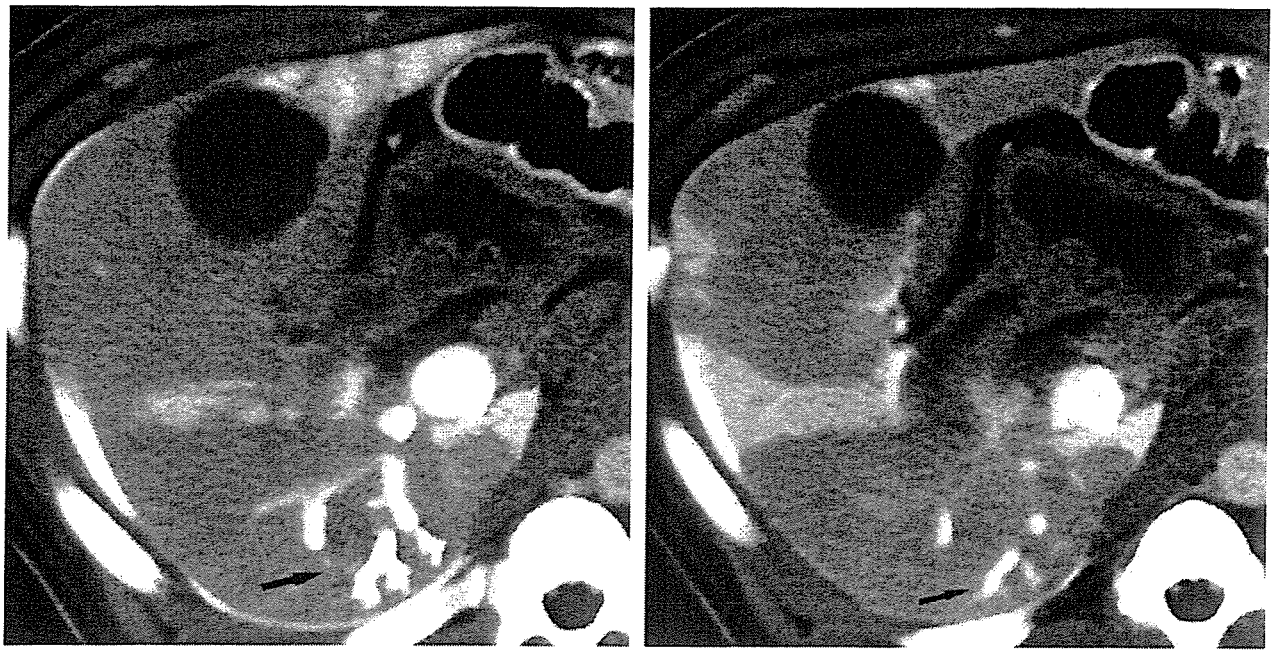

Fig. 2. PVE of the anterior portal branches of the right lobe. A. Early-phase CTAP with wedge infusion during balloon occlusion demonstrates the dilated embolized portal branches (*arrow*). B. Late-phase CTAP shows slight obliteration of the embolized branches (*arrow*).

have a high nuclear-to-cytoplasm (N/C) ratio. Microscopic examination also revealed parenchymal damage and fibrosis 3–6 weeks after PVE. However, no significant changes were observed in either hepatic arteries or bile ducts at any time after PVE.

Discussion

The results of this study provide experimental evidence that a regenerative response and histopathologic changes in the liver with an increase of mean FLR/TELV follow PVE in pigs. The results also showed that the serum ethanol concentration after instillation was less than 0.51 mg/dl. These results suggest that this procedure is safe and followed by only a transient, low serum ethanol level.

PVE leads to atrophy of the lobe embolized and secondary hypertrophy of the unembolized lobes (3, 9, 13). The results of this study confirm the delay and extent of hypertrophy induced in the unembolized lobe and the feasibility of PVE. The results are consistent with the findings in previous studies of PVE effects in pigs (7). The lack of complications after PVE with absolute ethanol in this study may be explained by the fact that the balloon catheter prevented reflux of absolute ethanol.

In our study, no blood perfusion was observed in sinusoids of the embolized liver when the tissue was

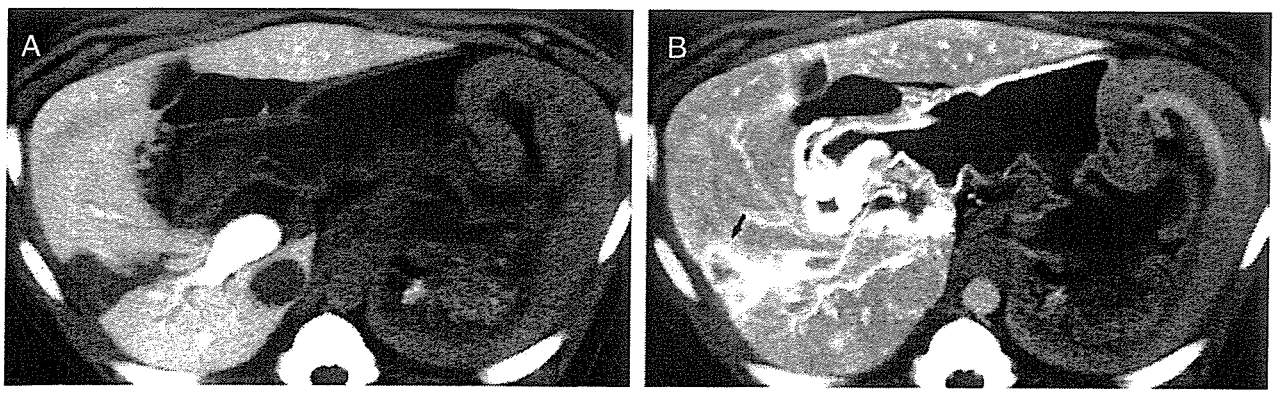

Fig. 3. PVE of the anterior portal branches of the right lobe. A. A perfusion defect was seen in the embolized liver on CTAP. The extent of the perfusion defects ranged from 76% to 100% of the embolized segment involved (grade 4). B. Parenchymal enhancement was observed in the embolized liver. Heterogeneous enhancement with central low attenuation was seen (*arrow*).

Acta Radiologica rad60237.3d 6/4/05 17:08:08

Fig. 4. PVE of the portal branches supplying segment IV. Periportal hyperattenuation of the embolized portal branches was observed on CTAP (*arrows*). The extent of periportal hyperattenuation was less than or equal to 25% of the embolized segment involved (grade 1).

fixated with absolute ethanol. Nevertheless, our observations conflict with the findings of previous studies suggesting that absolute ethanol is advantageous as a destructive embolizing agent for liver tissue in rats (7, 8). The investigators reported that the thrombi allowed incomplete obstruction or recanalization of vessels in the short term after PVE. This apparent discrepancy must be attributable to the procedure used to infuse absolute ethanol during balloon occlusion. Our results seem to suggest that dilution occurs more readily and the affected tissue is more likely to be fixated by absolute ethanol.

Significant increases in the serum concentrations of alanine aminotransferase and lactic acid dehydrogenase were observed in our study. The relationship between the concentrations of substances measured in the serum samples and areas of PVE showed that the serum concentration of alanine aminotransferase depended on the interval after PVE. The serum lactic acid dehydrogenase concentration was also dependent on the interval after PVE. Both values peaked at a level less than three times the baseline value 1–3 days after PVE and returned to the baseline value at 7–10 days (16). The serum transaminase concentrations rose in proportion to the dose of absolute ethanol injected in dogs

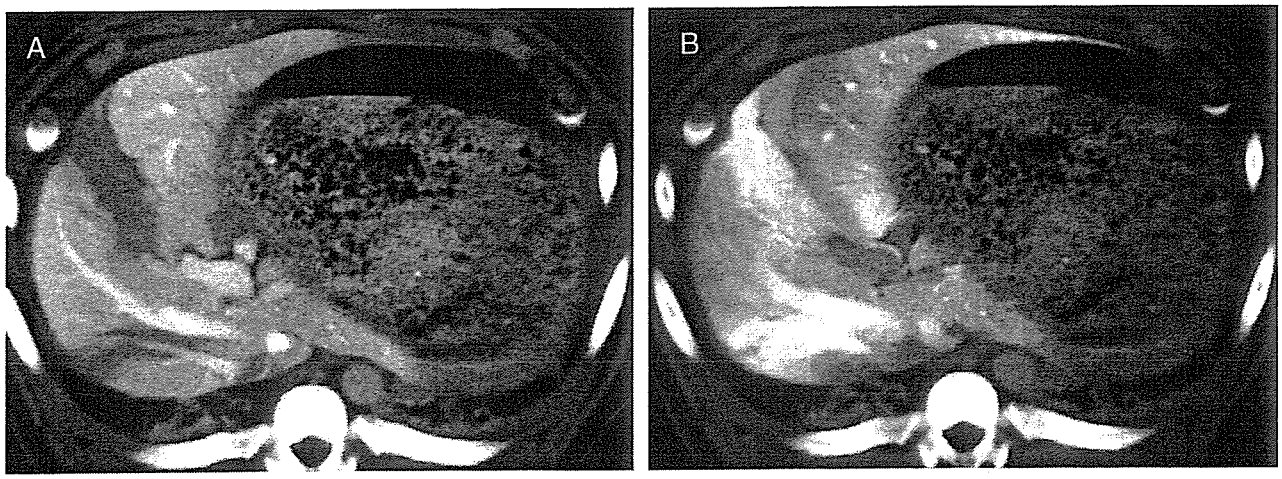

Fig. 5. Six weeks after PVE of the anterior portal branches. A. Perfusion defects with severe atrophy of the embolized liver were identified on CTAP, and the grade was 4. B. CTHA showed parenchymal enhancement corresponding to the perfusion defects on CTAP.

Table 1. Changes of serum concentration of blood samples after PVE

	Pre-PVE	Post-PVE	*P* value
ALT (U/L)	33.1±7.2 (25–48)	400.7±185.4 (70–691)	<0.05
AST (U/L)	56.7±26.2 (34–121)	66.8±25.8 (44–112)	ns
Total bilirubin (mg/dl)	0.01±0.03 (0.00–0.10)	0.02±0.04 (0.00–0.10)	ns
LDH (U/L)	808.5±276.1 (447–1461)	1279.7±717.4 (582–2945)	<0.05
ALP (U/l)	237.0±45.3 (173–325)	249.0±51.1 (170–325)	ns
Creatinin (mg/dl)	0.91±0.10 (0.76–1.02)	0.93±0.20 (0.79–1.12)	ns

ALT=Alanine aminotransferase, AST=asparate aminotransferase, LDH=lactic acid dehydrogenase, ALP=alkaline phosphatase.
All values after PVE were measured on the day of sacrifice.
ns=not significant.
Changes in serum concentration of blood samples were assessed using the Friedman test.

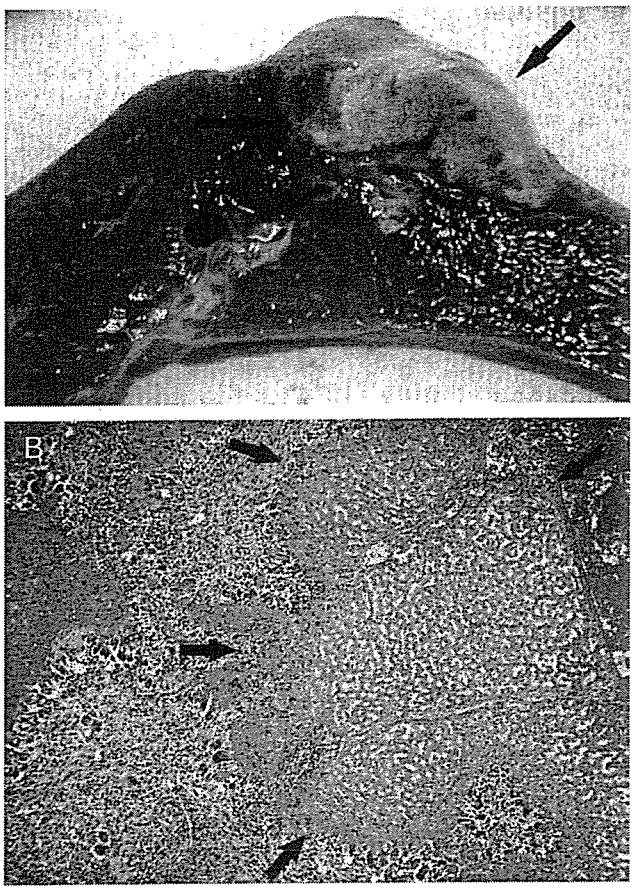

Fig. 6. A. Cut surface of a specimen of the embolized liver 3 weeks after PVE shows yellowish mass-like areas adjacent to Glisson's capsule (*arrows*). B. Numerous degenerated hepatocytes are identified but the lobular architecture of the liver is preserved (*arrows*).

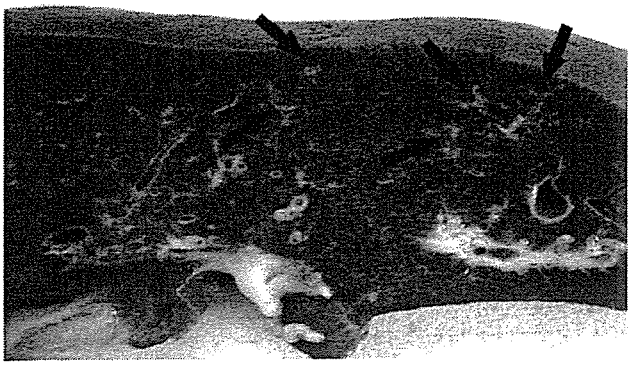

Fig. 7. Cut surface of a specimen of the embolized liver 3 weeks after PVE demonstrates yellowish amorphous areas in Glisson's capsule (*arrows*).

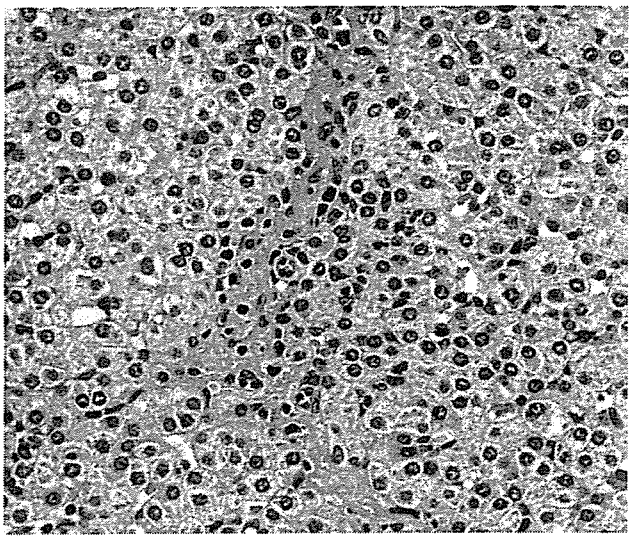

Fig. 8. Degenerated hepatocytes in the embolized lobes are more likely to be eosinophilic and to have a high nucleus-to-cytoplasm (N/C) ratio.

(22). The significant and transient increases in transaminases after PVE may be explained by extensive peribiliary inflammation and hepatic necrosis observed histopathologically. The increases were caused by massive cell destruction by ethanol, and the clearance of the enzymes was rapid and correlated with the fast reabsorption of the necrotic tissue observed pathologically. The serum ethanol concentration increased within the first 3 min after injection in every animal. PVE with absolute ethanol is associated with minimal side effects and is considerably less toxic.

Table 2. The difference of serum concentration of blood samples between segmental and susegmental PVE

	Segmental PVE	Subsegmental PVE	*P* value
ALT post-pre (U/L)	352.5±83.7	390.3±91.1	ns
AST post-pre (U/L)	10.2±6.9	10.0±2.6	ns
Total bilirubin post-pre (mg/dl)	0.02±0.02	0	ns
LDH post-pre (U/L)	592.7±245.7	289.0±109.1	<0.05
ALP post-pre (U/l)	9.3±20.9	16.0±7.3	ns
Creatinin post-pre (mg/dl)	0.04±0.03	0.06±0.03	ns

Data are presented as post-PVE minus pre-PVE. ALT=Alanine aminotransferase, AST=asparate aminotransferase, LDH=lactic acid dehydrogenase, ALP=alkaline phosphatase.
ns=not significant.
The diffence of serum concentration of blood samples between segmental or subsegmental PVE was assessed by two-way analysis of variance (ANOVA).

Since ethanol only causes tissue necrosis above a certain concentration, it must be delivered to the target segment of the liver without systemic dilution. To achieve this, we rapidly and forcibly injected ethanol via a catheter wedged into the portal vein, thereby obstructing portal blood flow to the target segment. There is a paucity of information on the systemic effects of absolute ethanol after PVE (1). The results of the present study are consistent with previous results and revealed that this procedure is safe and associated with only a transient appearance of low ethanol levels in serum.

Ethanol causes tissue fixation, sludging of blood cells, and protein denaturation and coagulation. In our study, the portal veins dilated and thrombosed when they came into contact with ethanol. Animal studies (10, 20, 22) of portal vein occlusion have shown that the hepatocytes in the embolized lobes undergo apoptosis. Hepatocyte apoptosis is likely to explain the minimal alterations in liver function tests observed in human studies (7, 8). However, no hepatocyte apoptosis was observed in the embolized lobes in our study. Our findings were attributable to tissue fixation by absolute ethanol that induced hepatocytes degeneration without destruction of the lobular architecture of the embolized lobe. Therefore, damage to hepatocytes by tissue fixation may result in parenchymal necrosis.

The safety of the PVE procedure may allow expansion of its indications to patients with insufficient remnant liver volume. It has been hypothesized that liver regeneration is attributable to the ability of hepatocytes to dedifferentiate and expand clonally (1). Intrahepatic and extrahepatic factors may also contribute to the induction and control of hepatocyte growth (13). Additional randomized study of the PVE procedure will improve our understanding of the mechanisms in liver regeneration.

In conclusion, a regenerative response and histopathologic changes in the liver follow PVE in pigs. The induction of liver necrosis can be well controlled and these changes are followed by a regenerative response in the remnant liver.

References

1. Abdalla EK, Hicks ME, Vauthey JN. Portal vein embolization: rationale, technique, and future prospects. Br J Surg 2001;88:165–75.
2. Azoulay D, Raccuia JS, Castaing D, Bismuth H. Right portal vein embolization in preparation for major hepatic resection. J Am Coll Surg 1995;181:267–9.
3. Azoulay D, Castaing D, Smail A, Adams R, Cailliez V, Laurent A, et al. Resection of nonresectable liver metastases from colorectal cancer after percutaneous portal vein embolization. Ann Surg 2000;231:480–6.
4. Cheng Y, Kan Z, Chen C, Huang T, Chen T, Tang B, et al. Efficacy and safety of preoperative lobar or segmental ablation via transarterial administration of ethiodol and ethanol mixture for treatment of hepatocellular carcinoma: clinical study. World J Surg 2000;24:844–50.
5. de Baere T, Roche A, Elias D, Lasser P, Lagrange C, Bousson V. Preoperative portal vein embolization for extension of hepatectomy indications. Hepatology 1996;24:1386–91.
6. de Baere T, Roche A, Vavasseur D, Therasse E, Indushekar S, Elias D, et al. Portal vein embolization: utility for inducing left hepatic lobe hypertrophy before surgery. Radiology 1993;188:73–7.
7. Duncan JR, Hick ME, Cai SR, Brunt EM, Ponder KP. Embolization of portal vein branches induces hepatocyte replication in swine: a potential step in hepatic gene therapy. Radiology 1999;210:467–77.
8. Ikeda K, Kinoshita H, Hirohashi K, Kubo S, Kaneda K. The ultrastructure, kinetics and intralobular distribution of apoptotic hepatocytes after portal branch ligation with special reference to their relationship to necrotic hepatocytes. Arch Histol Cytol 1995;58:171–84.
9. Imamura H, Shimada R, Kubota M, Matsuyama Y, Nakayama A, Miyagawa S, et al. Preoperative portal vein embolization: an audit of 84 patients. Hepatology 1999;29:1099–105.
10. Kaminou T, Nakamura K, Onoyama Y, Fujimoto T. Experimental selective segmental ablation of rat liver by transportal ethanol injection. Eur Radiol. 6, 502–9.
11. Kawasaki S, Makuuchi M, Miyagawa S, Kakazu T. Radical operation after portal embolization for tumor of hilar bile duct. J Am Coll Surg 1994;178:480–6.
12. Kinoshita H, Sakai K, Hirohashi K, Igawa S, Yamasaki O, Kubo S. Preoperative portal vein embolization for hepatocellular carcinoma. World J Surg 1986;10:803–8.
13. Kubota K, Makuuchi M, Kusaka K, Kobayashi T, Miki K, Hasegawa K, et al. Measurement of liver volume and hepatic functional reserve as a guide to detection-making in resectional surgery for hepatic tumors. Hepatology 1997;26:1176–81.
14. Lee KC, Kinoshita H, Hirohashi K, Kubo S, Isawa R. Extension of surgical indications for hepatocellular carcinoma by portal vein embolization. World J Surg 1993;17:109–15.
15. Lu MD, Liang LJ, Huang JF, Ye WJ, Yang QS, Peng BG, et al. Portal vein embolization with ethanol injection via a fine needle in dogs. Surg Today 1995;25:416–20.
16. Madoff DC, Hick ME, Abdalla EK, Morris JS, Vauthey JN. Portal vein embolization with polyvinyl alcohol particles and coils in preparation for major liver resection for hepatobiliary malignancy: safety and effectiveness study in 26 patients. Radiology 2003;227:251–60.
17. Makuuchi M, Thai BL, Takayasu K, Takayama T, Kosuge T, Gunyen P, et al. Preoperative portal embolization to increase safety of major hepatectomy for hilar bile duct carcinoma: a preliminary report. Surgery 1990;107:521–7.
18. Nagino M, Kamiya J, Kanai M, Uesaka K, Sano T, Yamamoto H, et al. Right trisegment portal vein

embolization for biliary tract carcinoma: technique and clinical utility. Surgery 2000;127:155–60.
19. Nagino M, Nimura Y, Kamiya J, Kondo S, Uesaka K, Kin Y, et al. Right or left trisegment portal vein embolization before hepatic trisegmentectomy for hilar bile duct carcinoma. Surgery 1995;117:677–81.
20. Ogasawara K, Uchino J, Une Y, Fujioka Y. Selective portal vein embolization with absolute ethanol induces hepatic hypertrophy and makes more extensive hepatectomy possible. Hepatology 1996;23:338–45.
21. Shimamura T, Nakajima Y, Une Y, Namieno T, Ogasawara K, Yamashita K, et al. Efficacy and safety of preoperative percutaneous transhepatic portal embolization with absolute ethanol: a clinical study. Surgery 1997;121:135–41.
22. Yamakado K, Takeda K, Nishide Y, Jin J, Matsumura A, Hirano T, et al. Portal vein embolization with steel coils and absolute ethanol: a comparative experimental study with canine liver. Hepatology 1995;22:1812–8.

Available online at www.sciencedirect.com
SCIENCE DIRECT®
Biomaterials
ELSEVIER
Biomaterials 26 (2005) 3327–3331
www.elsevier.com/locate/biomaterials

Technical note

Size control of calcium alginate beads containing living cells using micro-nozzle array

Shinji Sugiura[a,b,c], Tatsuya Oda[d,e], Yasuhiko Izumida[a], Yasuyuki Aoyagi[d], Mitsuo Satake[f], Atsushi Ochiai[e], Nobuhiro Ohkohchi[d], Mitsutoshi Nakajima[a,*]

[a]*Food Engineering Division, National Food Research Institute, 2-1-12 Kannondai, Tsukuba, Ibaraki 305-8642, Japan*
[b]*The Organization for Pharmaceutical Safety and Research, 3-3-2 Kasumigaseki, Chiyoda-ku, Tokyo 100-0013, Japan*
[c]*Radiology Division, National Cancer Center Hospital East, 6-5-1 Kashiwanoha, Kashiwa, Chiba 277-8577, Japan*
[d]*Department of Surgery, Institute of Clinical Medicine, University of Tsukuba, 1-1-1 Tennoudai, Tsukuba, Ibaraki 305-8575, Japan*
[e]*Pathology Division, National Cancer Center Research Institute East, 6-5-1 Kashiwanoha, Kashiwa, Chiba 277-8577, Japan*
[f]*Diagnostics Radiology Division, National Cancer Center Hospital, 5-1-1 Tsukiji, Chuo Ku, Tokyo 104-0045, Japan*

Received 9 April 2004; accepted 26 August 2004
Available online 30 September 2004

Abstract

Size-controlled small (i.e. less than 300 μm) polyelectrolyte complex gel beads are urgently desired for wide-spread application, including use in medical, pharmaceutical, and bioengineering fields. However, it was impossible to obtain smaller beads less than 300 μm with conventional apparatuses. We developed a novel microfluidics device that utilizes silicon micro-nozzle (MN) array, enabling to produce 50–200 μm calcium alginate beads with a narrow size distribution. Alginate aqueous solution was extruded through a precisely fabricated thin (30 μm × 30 μm) and short (500 μm) MN and was sheared by the viscous drag force of oil flow to form alginate droplets. Alginate droplets were immediately reacted with $CaCl_2$ droplets at the downstream of oil flow to form calcium alginate gel beads. This device enabled us to successfully encapsulate living cells into 162 μm calcium alginate beads with maintaining viability, which was confirmed by the expression of marker protein.

Keywords: Alginate; Cell encapsulation; Microcapsule; Micromachining; Microstructure; Size control

1. Introduction

Spherical gel beads containing living cells have been applied in the transplantation of pancreatic islet into diabetic animals [1,2], treatment of hormone or protein deficient diseases [3], and cancer therapy [4–6]. Another utilization includes microcarriers [7], scaffold [8] for cell cultures and tissue engineering [9]. As gel materials, polyelectrolyte complex systems have often been used. Among them, calcium alginate is the most commonly employed system for its easiness in gel formation. Once liquid alginate solutions are contacted with polycation (Ca^{2+}), they immediately transformed into gel by binding between guluronic acid blocks in alginate and Ca^{2+}.

Smaller beads offer many advantages, such as better transportation of nutrients and oxygen [10], better dispersion, better mechanical strength, easier implantation, and potential access to new implantation sites [11]. Widely used production techniques for preparing polyelectrolyte complex gel beads include the vibrating nozzle method and coaxial air-flow method [12]. Calcium alginate beads with 300–800 μm diameters have been successfully prepared using these methods. Though preparation of smaller beads with 170 μm diameter was reported through the electrostatic droplet generation

*Corresponding author. Tel.: +81-298-38-7997; fax: +81-298-38-8122.
E-mail address: mnaka@affrc.go.jp (M. Nakajima).

0142-9612/$ - see front matter © 2004 Elsevier Ltd. All rights reserved.
doi:10.1016/j.biomaterials.2004.08.029

method [13], the beads possess a wide size distribution with a standard deviation of 70 μm. Preparation of smaller beads of less than 300 μm with a narrow size distribution has been impractical to date, due particularly to nozzle diameter limitations, the narrowest being a 250 μm outer diameter for a 31 gauge needle. Furthermore, productivity decreases drastically when thinner needles are used because of the high-pressure loss.

The application of micromachining techniques has increased rapidly in biotechnology in the last decade [14,15]. We recently proposed a novel device for preparing monodispersed emulsion droplets from 3 to 100 μm using a microfabricated channel array [16–18]. We demonstrate in this study a novel microfluidics device that utilizes a silicon micro-nozzle (MN) array, enabling to prepare 50–200 μm calcium alginate beads. Sodium alginate aqueous solution was extruded into the laminar flow of soybean oil through an MN, and size-controlled alginate droplets were formed. Alginate droplets were immediately reacted with $CaCl_2$ droplets to form calcium alginate beads.

2. Materials and methods

2.1. Experimental setup for alginate beads formation

The laboratory-scale apparatus for beads formation, which is depicted in Fig. 1, was similar to the apparatus for emulsion formation [19]. The MNs were fabricated by photolithography and the two-step deep reactive ion-etching process [19]. The MN has an inner width of 30 μm, an outer width of 60 μm, and a nozzle height of 15 μm. The flow channels inside the MNs are fabricated through a 500-μm-thick silicon plate.

2.2. Alginate beads formation

Sodium alginate (IL-2) was kindly provided from Kimica Corp. (Tokyo, Japan) and dissolved in HEPES buffered saline at the concentration of 1.5%. Soybean oil was purchased from Wako Pure Chemical, Ind. (Osaka, Japan). Alginate solution was fed into the flow of soybean oil through the MN in the upper stream of the soybean oil flow, and $CaCl_2$ 0.1 M aqueous solution containing 0.14 M NaCl was fed through MN in the downstream area of the oil flow as shown in Fig. 1c. The formed alginate droplets and $CaCl_2$ droplets collide with each other in the stream of soybean oil, and the reaction between the alginate and Ca^{2+} proceeds by coalescence of the droplets. No surfactant was added in the system to promote coalescence.

For encapsulating living cells, a 1.5% sodium alginate solution containing cells at 1×10^7 cells/ml

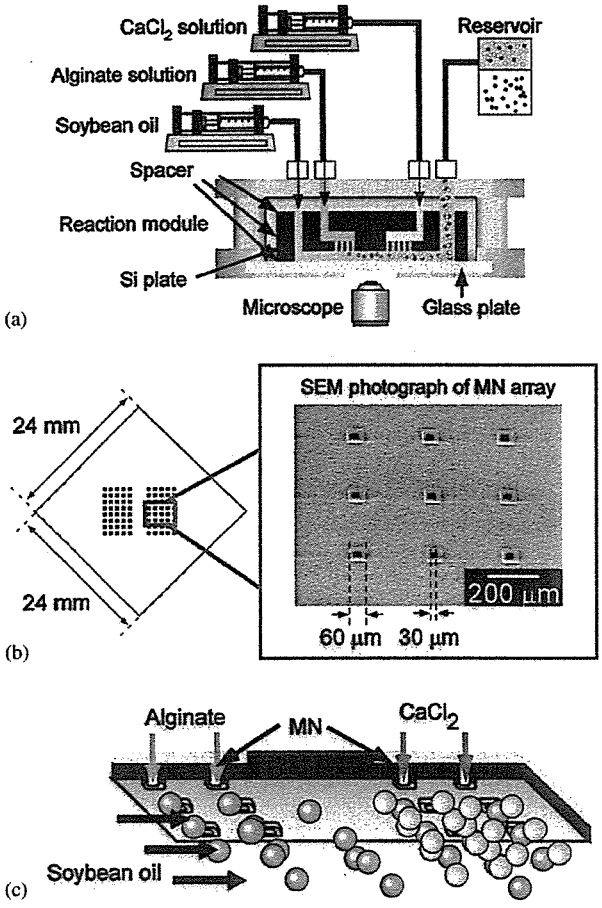

Fig. 1. Equipment for the alginate beads formation system and schematics of the beads preparation process. (a) Schematics of the experimental equipment. (b) Schematics of the silicon plate and SEM photograph of the MN array fabricated on a silicon plate. (c) Schematic flows in the reaction module.

was extruded through the MNs into the oil flow to prepare alginate beads. The calcium alginate beads were formed as described above, and treated with lipase solution containing 0.1% lipase (Amano PS, Amano Enzyme Inc., Aichi, Japan) at 37 °C for 10 min, and washed with washing buffers ($CaCl_2$ solution and HBS).

2.3. Cell culture

Human kidney 293 cells were obtained from the Japan health science foundation (Tokyo, Japan) and transfected with pIRES2-EGFP vector (Clontech Laboratories, Inc., Palo Alto, CA, USA) encoding GFP using an adenovirus. The transfected cells (293/GFP) were cultured in Dulbecco's modified Eagle medium (DMEM; Sigma-Aldrich Co., St. Louis, MO, USA) supplemented with 10% heat-inactivated fetal bovine serum (Sigma-Aldrich Co.).

2.4. Measurement and analytical method

Scanning electron microscopy photographs were taken with a JSM-5600LC (JEOL Ltd., Tokyo, Japan). The number-average diameters (D [μm]) and coefficients of variation (CV [%]; percentage of standard deviation) of the droplets/beads were determined from pictures of 100 droplets/beads. Average values of roundness (R) were used to evaluate the shape of the prepared beads, which is defined as

$$R = \frac{4\pi S}{L^2}, \quad (1)$$

where S is the projection area of beads and L is the perimeter of the beads. Winroof (Mitani Corporation, Fukui, Japan) software was used to analyze the captured images.

3. Results

3.1. Droplet formation process from MN

Sodium alginate aqueous solution was extruded into the flow of soybean oil through an MN. The oil flow rates were 200 and 1000 ml/h, corresponding to flow velocities of 26 and 128 mm/s. The flow rate of the alginate solution was identical in both series. That is 5 ml/h, corresponding to flow velocities of 15 mm/s in each nozzle. One hundred and four nozzles produce alginate droplets in the present system. The alginate solution fed from the MN was sheared by the flow of soybean oil and monodispersed droplets were formed as shown in Figs. 2a and b. Smaller droplets were formed in a faster flow velocity of the soybean oil because of the higher viscous drag force. The number-average diameters and CVs of the droplets were 247 μm and 5.0% for 26 mm/s flow velocity and 88.4 μm and 5.9% for 128 mm/s flow velocity. The Reynold's numbers in these experimental conditions were 0.25 and 1.23, which means oil flow was laminar flow.

3.2. Beads formation process

The prepared alginate droplets were required to react with $CaCl_2$ solution for gel formation. $CaCl_2$ aqueous solution was extruded through the MN at the downstream area of the oil flow at the flow rate of 100 ml/h, which is 20 times greater than that of the alginate solution. The excess amount of $CaCl_2$ solution compared to alginate solution is expected to prevent coalescence between the alginate droplet and alginate droplet. Calcium alginate beads were formed by reaction between the alginate droplets and $CaCl_2$ droplets. Most of the prepared beads had spherical or ellipsoidal shapes

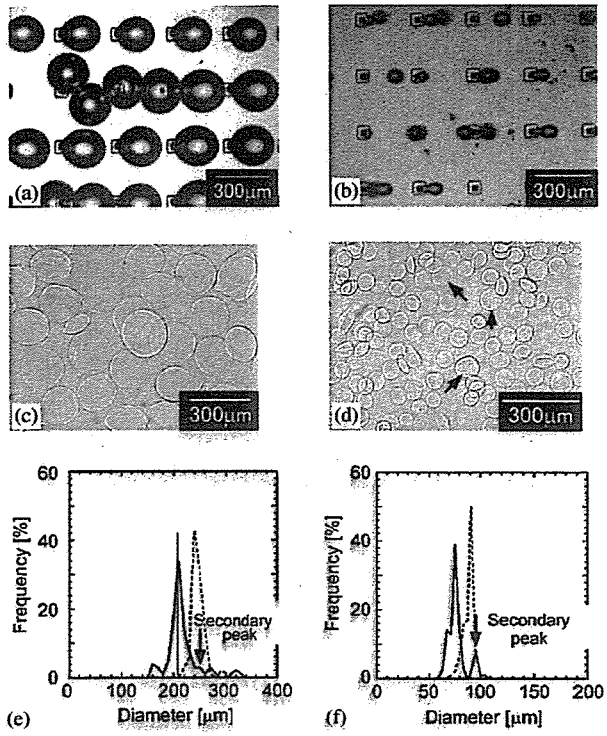

Fig. 2. Droplet formation process and prepared calcium alginate beads at different flow velocities of soybean oil. Microscope photographs of the alginate droplet formation process for: (a) 26 mm/s flow velocities of soybean oil during droplet formation process and (b) 128 mm/s flow velocities of soybean oil. Microscope photographs of prepared alginate beads for: (c) 26 mm/s flow velocities of soybean oil during droplet formation process and (d) 128 mm/s flow velocities of soybean oil during droplet formation process. The beads 1.25 times larger than the mean values (two times larger in volume) were observed (arrows in (d)). Diameter distribution of droplets and beads for: (e) 26 mm/s flow velocities of soybean oil and (f) 128 mm/s flow velocities of soybean oil. The liquid droplet diameter distributions are indicated by the dotted line, and the gel-bead diameter distributions are indicated by the solid line. The secondary peaks 1.25 times larger than the mean values (two times larger in volume) were observed (arrows in (e, f)).

as shown in Figs. 2c and d. The values of roundness of the prepared beads were 0.95 for 26 mm/s of oil flow and 0.97 for 128 mm/s of oil flow. Figs. 2e and f illustrate the changes in diameter distribution between the liquid droplets before gelation and gel beads after gelation. The number-average diameters and CVs of the prepared beads were 216 μm and 14.4% for 26 mm/s of oil flow and 77.4 μm and 11.1% for 128 mm/s of oil flow. The droplet's diameter had decreased by 13% from their original droplet diameter after bead formation in each case. Secondary peaks were observed at values 1.25 times greater than the mean values, which correspond to twice as much volume (Figs. 2e and f). Some of the alginate droplets may coalesce with each other before coalescence with the $CaCl_2$ solution. The coefficients of variation of the prepared beads were slightly increased,

but the prepared beads maintained a narrow diameter distribution after bead formation.

The bead formation system proposed in this study can be applied for encapsulation of living cells, since the system works under sterile conditions. Human fetal kidney 293/GFP cells were entrapped in the calcium–alginate beads using the MN system. The flow velocity of the oil was 103 mm/s. The flow rate of the alginate solution was 10 ml/h, and the flow rate of the $CaCl_2$ solution was 100 ml/h. Cell-containing calcium alginate beads were successfully prepared using MN system as depicted in Fig. 3. The prepared alginate beads were easily dispersed in the aqueous solution after lipase treatment. The number-average diameters and coefficients of variation of the prepared droplets and beads were 169 μm and 8.0% for droplets and 162 μm and 28% for beads. Several beads appeared fragmented in Fig. 3. In our observation, 11% of the prepared beads had neither spherical nor ellipsoidal shape, which had been fragmented or deformed. Green fluorescence from the GFP produced by the cells entrapped in the alginate beads is depicted in Fig. 3b, indicating that living cells were successfully encapsulated in the calcium alginate beads.

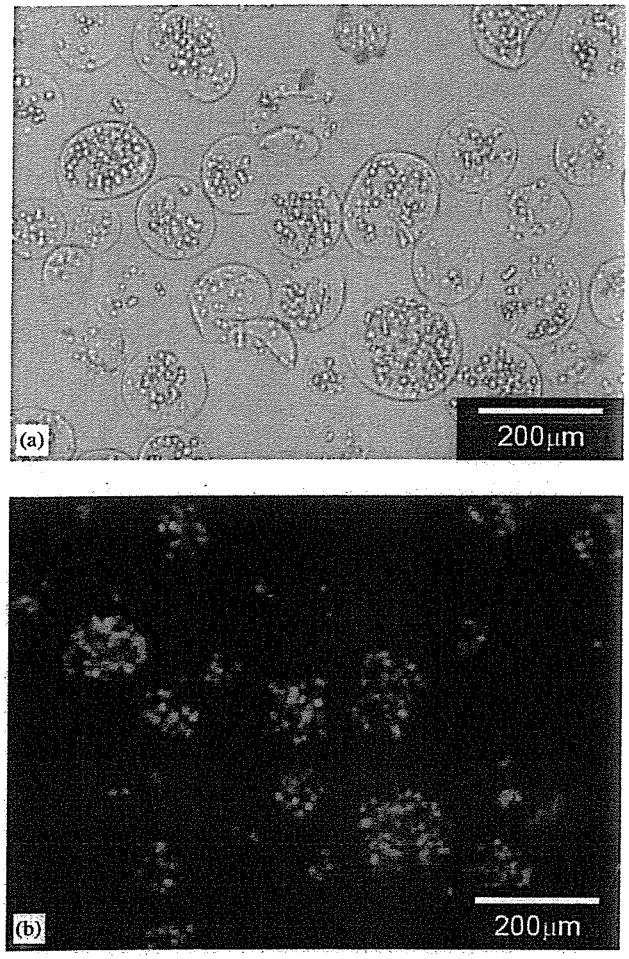

Fig. 3. Cell encapsulation into calcium alginate beads. Microscope photographs of calcium alginate beads containing 293/GFP cells observed in a bright field (a) and fluorescence mode (b).

4. Discussion

The MN described here has a thinner and shorter structure than commercially available needles (typically with an outer diameter of 250 μm and needle length of 12.7 mm for 31 gauge and 1/2 in needle), which is advantageous in terms of preciseness and low-pressure loss. The device utilizes the features of microfluidics (i.e. significant viscous force and laminar flow) and it leads to stable shearing during droplet formation. The droplet–droplet reaction system demonstrated in this study has the advantages of a large surface area of reaction liquid, which creates an opportunity for an immediate reaction between the alginate droplet and $CaCl_2$ solution. The above advantages enable the beads prepared in this study to be smaller and have a narrower diameter distribution compared to conventional methods.

The productivity of alginate beads was determined by the flow rate of the alginate solution. Stable droplet formation was possible in the present system up to an alginate flow rate of 20 ml/h using one hundred and four nozzles. The productivity of alginate droplets from the unit silicon plate area was 214 ml/(cm^2 h). The low-pressure loss structure of the device leads to high productivity as an air-flow method and electrostatic droplet generation method despite the present small-scale apparatus. Though the productivity with the vibrating nozzle method (i.e. 600 ml/h) [20] is higher than the present system, it may decrease for preparing beads smaller than 300 μm because of the high-pressure loss caused by the thin needle. The scale-up of productivity to 1000 times would be possible by utilizing a large silicon plate and an accumulation of multiple silicon plates. Therefore, we believe that the productivity of the present system is sufficiently high for us to overcome the limitation of productivity by scale-up.

The nozzle-type exit shape is beneficial especially in producing alginate beads containing biological cells. It prevents wetting of the silicon plate surface with the dispersed aqueous phase. This leads to better droplet detachment, which is important for continuous shearing and stable droplet formation. The beads were formed under sterile conditions and without chemically irritant materials such as surfactant, which enabled successful encapsulation of living cells in the alginate beads. The viability of the entrapped cells in Fig. 3 is roughly estimated as 70%. The CV for beads containing cells increased. Inhomogeneous structure of the cell containing alginate solution affected the droplet formation

process and led to the formation of a different sized droplet. Substances secreted from the cells would disturb the coalescence between alginate droplets and $CaCl_2$ droplets. The alginate beads of 50–200 μm with a narrow size distribution are useful carriers for cell immobilization since they provide better transportation of nutrients and oxygen. The beads prepared by this method would be useful as sophisticated biomaterials; for example, as cell transplantation carriers, drug carriers, and scaffold for tissue engineering and cell cultures because of their characteristic physical, chemical, and biological properties.

5. Conclusions

We presented here a novel microfabricated device enabling to prepare size-controlled small calcium alginate beads less than 300 μm. The unique characteristics of our device include (a) a thin (30 μm × 30 μm) and short (500 μm) silicon nozzle, (b) droplet formation by viscous drag force of the oil flow, (c) a droplet–droplet reaction for gel formation, and (d) a nozzle-type exit shape (but not a flat exit pore). Using this device, the alginate beads with diameters of 50–200 μm and coefficients of variation of less than 15% were successfully prepared. The living cells were successfully encapsulated into 162 μm calcium alginate beads with maintaining viability. The smaller alginate beads of 50–200 μm prepared by this device are expected to be used in various fields, including medical, pharmaceutical, and bioengineering fields.

Acknowledgments

We thank Dr. T. Maruyama (Kyushu University) for useful information about lipase. We thank Mr. Y. Sando (Konica Minolta Holdings, Inc.) for helping with fabrication of the silicon plate. This work was supported by the Nanotechnology Project, Ministry of Agriculture, Forestry and Fisheries, and the Program for Promotion of Fundamental Studies in Health Sciences of the Organization for Pharmaceutical Safety and Research of Japan.

References

[1] Lim F, Sun AM. Microencapsulated islets as bioartificial endocrine pancreas. Science 1980;210:908–10.
[2] De Vos P, Van Hoogmoed CG, Van Zanten J, Netter S, Strubbe JH, Busscher HJ. Long-term biocompatibility, chemistry, and function of microencapsulated pancreatic islets. Biomaterials 2003;24:305–12.
[3] AlHendy A, Hortelano G, Tannenbaum GS, Chang PL. Growth retardation—an unexpected outcome from growth hormone gene therapy in normal mice with microencapsulated myoblasts. Hum Gene Ther 1996;7:61–70.
[4] Read TA, Sorensen DR, Mahesparan R, Enger PØ, Timpl R, Olsen BR, Hjelstuen MHB, Haraldseth O, Bjerkvig R. Local endostatin treatment of gliomas administered by microencapsulated producer cells. Nat Biotechnol 2001;19:29–34.
[5] Joki T, Machluf M, Atala A, Zhu JH, Seyfried NT, Dunn IF, Abe T, Carroll RS, Black PM. Continuous release of endostatin from microencapsulated engineered cells for tumor therapy. Nat Biotechnol 2001;19:35–9.
[6] Cirone P, Bourgeois JM, Chang PL. Antiangiogenic cancer therapy with microencapsulated cells. Hum Gene Ther 2003;14:1065–77.
[7] Kwon YJ, Peng CA. Calcium-alginate gel bead cross-linked with gelatin as microcarrier for anchorage-dependent cell culture. Biotechniques 2002;33:212–8.
[8] Wang L, Shelton RM, Cooper PR, Lawson M, Triffitt JT, Barralet JE. Evaluation of sodium alginate for bone marrow cell tissue engineering. Biomaterials 2003;24:3475–81.
[9] Stevens MM, Qanadilo HF, Langer R, Shastri VP. A rapid-curing alginate gel system: utility in periosteum-derived cartilage tissue engineering. Biomaterials 2004;25:887–94.
[10] Chicheportiche D, Reach G. In vitro kinetics of insulin release by microencapsulated rat islets: effect of the size of the microcapsules. Diabetologia 1988;31:54–7.
[11] Leblond FA, Simard G, Henley N, Rocheleau B, Huet PM, Halle JP. Studies on smaller (−315 μM) microcapsules: IV. Feasibility and safety of intrahepatic implantations of small alginate poly-L-lysine microcapsules. Cell Transplant 1999;8:327–37.
[12] Dulieu C, Poncelet D, Neufeld RJ. Encapsulation and immobilization techniques. In: Kühtreiber WM, Lanza RP, Chick WL, editors. Cell encapsulation technology and therapeutics. Boston: Birkhäuser; 1999. p. 3–17.
[13] Bugarski B, Li Q, Goosen MFA, Poncelet D, Neufeld RJ, Vunjak G. Electrostatic droplet generation: mechanism of polymer droplet formation. AIChE J 1994;40:1026–31.
[14] Hong JW, Studer V, Hang G, Anderson WF, Quake SR. A nanoliter-scale nucleic acid processor with parallel architecture. Nat Biotechnol 2004;22:435–9.
[15] Meldrum DR, Holl MR. Microscale bioanalytical systems. Science 2002;297:1197–8.
[16] Sugiura S, Nakajima M, Iwamoto S, Seki M. Interfacial tension driven monodipersed droplet formation from microfabricated channel array. Langmuir 2001;17:5562–6.
[17] Kawakatsu T, Kikuchi Y, Nakajima M. Regular-sized cell creation in microchannel emulsification by vidual microprocessing method. J Am Oil Chem Soc 1997;74:317–21.
[18] Sugiura S, Nakajima M, Kumazawa N, Iwamoto S, Seki M. Characterization of spontaneous transformation-based droplet formation during microchannel emulsification. J Phys Chem B 2002;106:9405–9.
[19] Kobayashi I, Nakajima M, Chun K, Kikuchi Y, Fujita H. Silicon array of elongated through-holes for monodisperse emulsion droplets. AIChE J 2002;48:1639–44.
[20] Brandenberger HR, Widmer F. Immobilization of highly concentrated cell suspensions using the laminar jet breakup technique. Biotechnol Progr 1999;15:366–72.

Original Report

Ukihide Tateishi[1]
Tadashi Hasegawa[2]
Hiroaki Onaya[1]
Mitsuo Satake[1]
Yasuaki Arai[1]
Noriyuki Moriyama[1]

Myxoinflammatory Fibroblastic Sarcoma: MR Appearance and Pathologic Correlation

OBJECTIVE. The purpose of our study was to define the MR appearance of myxoinflammatory fibroblastic sarcoma of the soft tissues and to make correlations with the histopathologic features.

CONCLUSION. Myxoinflammatory fibroblastic sarcoma is an uncommon malignancy that typically affects adult subjects, who present with painless swelling. This lesion manifests on MR images as a poorly circumscribed mass involving the underlying tendon sheath in the distal extremities.

Myxoinflammatory fibroblastic sarcoma of the soft tissues is a rare low-grade tumor of uncertain origin that usually arises in the hands and feet. Myxoinflammatory fibroblastic sarcoma was first described in 1998 by Meis-Kindblom and Kindblom [1]. Montgomery et al. [2] named the tumor "inflammatory myxohyaline tumor" of the distal extremities with virocyte or Reed-Sternberg-like cells. Histologic characteristics are the spindle to epithelioid neoplastic cells as the manifestation of malignancy admixed with the myxoid and hyalinized matrix, the inflammatory infiltrate, and bizarre virocyte or Reed-Sternberg-like cells with enlarged vesicular nuclei [1–3].

More than 100 cases of myxoinflammatory fibroblastic sarcoma have been reported, with a large series identified in two articles [1–6]. However, MRI findings of myxoinflammatory fibroblastic sarcoma have rarely been documented. The purpose of this study was to characterize the MR appearance of myxoinflammatory fibroblastic sarcoma and to correlate that appearance with the histopathologic features.

Materials and Methods

MR images of all patients with pathologically proven myxoinflammatory fibroblastic sarcoma at our institution were retrospectively reviewed. Our institutional review board gave its approval for a review of patient records and images. The patients were identified by review of our institution's pathology database for a 2-year period. The affected patients included three males and one female who ranged in age from 15 to 62 years old (mean age, 35 years). All histopathologic specimens were reviewed by an experienced pathologist to confirm the diagnosis. Histopathologic examination in all patients showed spindle and epithelioid tumor cells with mild nuclear atypia. Ganglionlike cells and Reed-Sternberg-like cells were also prominent in all cases. Inflammatory cells, including neutrophils, lymphocytes, and eosinophils, were densely present in all cases. Immunohistochemistry was performed in all patients, and all tumors displayed immunoreactivity to vimentin, smooth-muscle actin, and CD34. These histopathologic characteristics were compatible with the diagnosis of myxoinflammatory fibroblastic sarcoma [7]. Medical records were reviewed by one of the authors for presenting complaints, disease progression, and outcome. Radiographs, available for all patients, were also evaluated by two radiologists for the presence of soft-tissue masses or nodules, mineralization, and bone destruction. The findings were recorded by consensus.

T1- and T2-weighted MR images were obtained in the sagittal and coronal planes using a surface coil. T1-weighted conventional spin-echo MR images were obtained using a 20-cm field of view, 3.5- to 5-mm section thickness, TR range/TE of 450–520/15, 160 × 256 matrix, and 2 signals acquired. T2-weighted fast spin-echo acquisitions with ($n = 3$) or without ($n = 1$) fat suppression were performed using a 20-cm field of view, 3.5- to 5-mm section thickness, 3,600–4,000/120, 160 × 256 ma-

Received June 2, 2004; accepted after revision July 28, 2004.

Supported in part by grant for Scientific Research Expenses for Health and Welfare Programs, The Foundation for the Promotion of Cancer Research, and second-term Comprehensive 10-year Strategy for Cancer Control.

[1]Division of Diagnostic Radiology, National Cancer Center Hospital and Institute, Tsukiji, Chuo-Ku, 104-0045, Tokyo, Japan. Address correspondence to U. Tateishi.

[2]Pathology Division, National Cancer Center Hospital and Institute, Tsukiji, Tokyo, Japan.

AJR 2005;184:1749–1753

0361–803X/05/1846–1749